Fate and origin of the quantum Otto heat engine based on the dissipative Dicke-Hubbard model

He-Guang Xu[1] and Shujie Cheng[2,3,*]

[1]*School of Physics and Optoelectronic Engineering, Guangdong Polytechnic Normal University, Guangzhou 510665, China*

[2]*Xingzhi College, Zhejiang Normal University, Lanxi 321100, China*

[3]*Department of Physics, Zhejiang Normal University, Jinhua 321004, China*

(Received 29 May 2026; revised 23 August 2026; accepted 15 October 2026; published 12 November 2026)

The Dicke-Hubbard model, describing an ensemble of interacting atoms in a cavity, provides a rich platform for exploring collective quantum phenomena. However, its potential for quantum thermodynamic applications remains largely uncharted. In this paper, a close connection between superradiance phase transition and the quantum thermodynamic applications of the Dicke-Hubbard model is established. Based on studies of the steady-state superradiant phase transition in the Dicke-Hubbard model and the thermodynamic mode of an Otto cycle with the Dicke-Hubbard model as the working substance, it is demonstrated that the steady-state synergistic mechanism under high- and low-temperature environments is the reason for the emergence of high-performance heat engines, while the competitive mechanism leads to the appearance of high-performance quantum refrigerators. A comparison of the thermodynamic behaviors of the Otto cycle with the Dicke model and the Dicke-Hubbard model as working substances reveals that the multicavity-coupled Dicke-Hubbard model achieves a higher coefficient of performance. These results not only deepen our understanding of the energy conversion mechanism in nonequilibrium quantum thermodynamics but also lay a theoretical foundation for the future experimental design of high-performance quantum Otto heat engines and refrigerators.

DOI: 10.1103/xftn-z5r1

I. INTRODUCTION

The burgeoning field of quantum thermodynamics seeks to extend the principles of classical thermodynamics to the quantum realm, revealing mechanisms for work extraction, refrigeration, and energy transduction [1,2]. Among various paradigms, the quantum Otto cycle stands as a fundamental and experimentally feasible model for a quantum heat engine [3,4]. By alternately coupling a quantum working substance to a hot and a cold bath during an isochoric process and modulating its Hamiltonian adiabatically, the cycle converts heat into useful work. The performance of such an engine is intrinsically tied to the quantum properties of the working substance—such as coherence, entanglement, and quantum criticality [5,6].

*Contact author: chengsj@zjnu.edu.cn

Published by the American Physical Society under the terms of the Creative Commons Attribution 4.0 International license. Further distribution of this work must maintain attribution to the author(s) and the published article's title, journal citation, and DOI.

Early theoretical and experimental studies have explored various systems as working substances. In the aspect of theoretical research, it involves single spins [7–9], bosonic substances [10], harmonic oscillators [11–13], few-level atoms [14,15], coupled spin systems [16–18], coupled spin-3/2 [19], relativistic oscillators [20], Bose-Einstein condensates [21,22], and light-matter systems described by the Jaynes-Cumming [23–26], quantum Rabi [27–32] models, anisotropic quantum Rabi-Stark model [33], and Dicke model (DM) [34]. In the aspect of experimental research, the quantum heat engines are realized in the platforms including superconducting circuits [35–39], trapped ion systems [11,12,40,41], optomechanics [7,42], ultracold atoms [43,44], and nuclear magnetic resonance [45–47].

While earlier findings provide foundational insights, the enhanced power output or unique quantum advantages caused by many-body physics are not fully demonstrated. Recently, there has been a growing interest in employing many-body systems, such as ultracold atoms in optical lattices [48] and interacting spin chains [49], where phenomena like superradiance and the Bose-Hubbard phase transition have been shown to significantly boost engine performance or induce new operational modes [50,51]. In fact, a growing number of theoretical studies have demonstrated that collective effects and many-body correlations can significantly enhance the performance of quantum heat engines and refrigerators [22,52–58]. Parallel experimental progress has also been made, with quantum heat engines realized in cold atomic systems [59,60]. These developments underscore the importance of understanding how collective light-matter interactions, such as those in the Dicke-Hubbard model (DHM), can be harnessed for quantum thermodynamic applications. Furthermore, the DM incorporates both many-body and superradiance physics as well, which describes an ensemble of two-level atoms collectively coupled to a single-mode cavity field [61]. This model exhibits a well-known superradiant quantum phase transition that can serve as a potent resource for quantum thermodynamics [62]. On the other hand, the Bose-Hubbard model, central to describing strongly correlated bosons in lattices, features a Mott insulator-to-superfluid transition [63]. The synthesis of these two models—the DHM [64,65]—creates a rich landscape where atomic hopping, on-site interactions, and collective light-matter coupling compete and intertwine. This hybrid system offers a unique test bed for investigating how the interplay between optical coherence and matter-wave correlations influences energy conversion processes. The DHM itself has been experimentally realized in a recent breakthrough [66], where a superradiant Mott insulator was observed, confirming the rich phase diagram of this system.

In recent years, although extensive research has been conducted on the equilibrium and nonequilibrium properties of the DHM, the potential of this model as a working substance for quantum heat engines has not been fully explored and exploited. Specifically, a crucial point is that the role of the superradiance phase transition in the working mode of thermodynamic cycles (such as the Otto cycle) remains unclear and lacks in-depth research. This unresolved issue further prompts us to explore a fundamental question in the field of quantum thermodynamics: What is the origin of quantum heat engines and refrigerators? In this work, we address this question by establishing a direct link between the steady-state quantum phases of the working substance and the resulting operating mode of the Otto cycle, as elaborated in Sec. IV. Furthermore, it is worth noting that the DHM is essentially a coupled system composed of multiple Dicke Models. Recent study [34] confirms that the single-cavity DM can be effectively used to design high-performance quantum Otto heat engines and refrigerators, which in turn leads us to a critical and research-worthy question: Can the inherent multicavity coupling mechanism of DHM enhance the performance of quantum heat engines and refrigerators beyond that of devices based on the single-cavity DM?

This paper is organized as follows. Section II introduces the DHM, the extended bosonic coherent state approach, and the quantum dressed master equation (DME). Section III introduces the quantum Otto cycle. Section IV presents the results of the DHM and discussions. The comparison between the DM and DHM is presented in Sec. V. A conclusion is made in Sec. VI.

II. MODEL AND METHOD

A. The Dicke-Hubbard model

The Hamiltonian describing the DHM consisting of a single-mode light field interacting with N identical two-level atoms and photon hopping between the nearest-neighboring cavity with the strength J, is expressed as [67–70] ($\hbar = 1$)

$$\hat{H} = \sum_i \hat{H}_i^{\text{Dicke}} - J\sum_{\langle i,j\rangle}(\hat{a}_i^\dagger \hat{a}_j + \hat{a}_j^\dagger \hat{a}_i), \tag{1}$$

where $\hat{H}_i^{\text{Dicke}}$ denotes the Hamiltonian of DM at ith site, and is given by ($\hbar = 1$) [71,72]

$$\hat{H}_i^{\text{Dicke}} = \omega_0 \hat{a}_i^\dagger \hat{a}_i + \Delta \hat{J}_z^i + \frac{2\lambda}{\sqrt{N}}(\hat{a}_i^\dagger + \hat{a}_i)\hat{J}_x^i, \tag{2}$$

where ω_0 and Δ are the frequencies of the single mode and atoms, respectively, λ is the atom-light coupling strength, $\hat{a}_i^\dagger(\hat{a}_i)$ denotes the creation (annihilation) operator of the bosonic field at ith site, $\hat{J}_x^i = \frac{1}{2}(\hat{J}_+^i + \hat{J}_-^i)$ and $\hat{J}_z^i$ are the pseudospin operators at ith site given by $\hat{J}_\pm^i = \sum_k^N \hat{\sigma}_\pm^{i,k}$, $\hat{J}_\alpha^i = \frac{1}{2}\sum_k^N \hat{\sigma}_\alpha^{i,k}$, with $\hat{\sigma}_\alpha$ ($\alpha = x, y, z$) being the Pauli operators. Index k labels atoms within the same cavity. The pseudospin operators satisfy the commutation relation $[\hat{J}_+^i, \hat{J}_-^i] = 2\hat{J}_z^i$, $[\hat{J}_z^i, \hat{J}_\pm^i] = \pm\hat{J}_\pm^i$, J describes the interaction strength of the intercavity hopping. The DM has been extensively studied due to its ability to undergo superradiance quantum phase transition at critical point $\lambda_c = \sqrt{\omega\Delta}/2$. It preserves the parity symmetry with parity operator $\hat{P} = \Pi_i \hat{P}_i$, where $\hat{P}_i = \exp\{i\pi\hat{\Lambda}_i\}$ is the parity operator of the ith site, and $\hat{\Lambda}_i = \hat{J}_z^i + \hat{a}_i^\dagger \hat{a}_i$ is the total excitation number.

B. Extended bosonic coherent state approach

We can transform the DHM to an effective single-site DM by using the mean-field approximation. Specifically, the intersite photon hopping term in Eq. (1) is decoupled as $\hat{a}_i^\dagger \hat{a}_j = \psi^* \hat{a}_i + \psi \hat{a}_j^\dagger - |\psi|^2$, with $\psi = \langle \hat{a} \rangle$ the superfluid order parameter. Therefore, the ith site Hamiltonian is given by

$$\hat{H}_i = \hat{H}_i^{\text{Dicke}} - zJ(\psi \hat{a}_i^\dagger + \psi^* \hat{a}_i) + zJ|\psi|^2, \tag{3}$$

where z is the number of nearest-neighbor sites, we set $z = 3$ for two-dimensional cavity lattice [68,71,73] in this paper. Since real order parameter is considered, i.e., $\psi = \psi^*$, the reduced model becomes site independent, resulting in the effective mean-field Hamiltonian ($\hat{H}_{\text{MF}}$)

$$\hat{H}_{\text{MF}} = \omega_0 \hat{a}^\dagger \hat{a} + \Delta \hat{J}_z + \frac{2\lambda}{\sqrt{N}}(\hat{a}^\dagger + \hat{a})\hat{J}_x - zJ\psi(\hat{a}^\dagger + \hat{a}) + zJ|\psi|^2, \tag{4}$$

where the order parameter ψ is obtained from the self-consistent iteration of the ground state.

The DM has numerically exact solution by using extended bosonic coherent state approach [74,75], which is used to obtain the numerical solution of Eq. (4) in a self-consistent way as well. At first, we introduce the angular momentum operator $\hat{J}_y$ to perform a rotation transformation on $\hat{H}_{\text{MF}}$, i.e., $\hat{H}_{\text{MF}}^s = \exp(i\pi\hat{J}_y/2)\hat{H}_{\text{MF}}\exp(-i\pi\hat{J}_y/2)$. Thus, we have

$$\hat{H}_{\text{MF}}^s = \omega_0 \hat{a}^\dagger \hat{a} - \frac{\Delta}{2}(\hat{J}_+ + \hat{J}_-) + (\hat{a}^\dagger + \hat{a})\left(\frac{2\lambda}{\sqrt{N}}\hat{J}_z - zJ\psi\right) + zJ\psi^2. \tag{5}$$

The corresponding eigenfunctions of $\hat{H}_{\text{MF}}^s$ can be expressed in terms of the basis $\{|\varphi_m\rangle_b \otimes |j, m\rangle\}$, $\{|j, m\rangle, m = -j, -j+1, \ldots, j-1, j\}$ ($j = N/2$) is the Dicke state for the two-level atoms. By using the extended bosonic coherent state (see Appendix A for detailed derivation), we finally obtain the eigenvalue equation

$$\omega_0\left(l - g_n^2 + zJ\psi^2\right)c_{n,l} - \Delta j_n^+ \sum_{k=0}^{N_{\text{tr}}} c_{n+1,kA_n}\langle l|k\rangle_{A_{n+1}} - \Delta j_n^- \sum_{k=0}^{N_{\text{tr}}} c_{n-1,kA_n}\langle l|k\rangle_{A_{n-1}} = E c_{n,l}, \tag{6}$$

where the coefficients are ${}_{A_n}\langle l|k\rangle_{A_{n-1}}=(-1)^l D_{l,k}$ and ${}_{A_n}\langle l|k\rangle_{A_{n+1}}=(-1)^k D_{l,k}$, with (see Appendix A for details)

$$D_{l,k}=e^{-G^2/2}\sum_{r=0}^{\min[l,k]}\frac{(-1)^r\sqrt{l!k!}G^{l+k-2r}}{(l-r)!(k-r)!r!}, \tag{7}$$

where $G=\frac{2\lambda}{\omega_0\sqrt{N}}$. In the following calculations, we select the truncation number $N_{\rm tr}=50$, which is sufficient to give the convergent excited state energies with relative error less than 10^{-5} as shown in Fig. 13. The behavior of the ground-state quantum phase transition of DHM was studied in Ref. [71] by using an extended coherent state approach within mean-field theory. Reference [76] investigated the quantum phase transition of light in the dissipative Rabi-Hubbard lattice under the framework of the mean-field theory.

C. Quantum dressed master equation

We study the dissipative DHM where the mean-field Dicke model for the ith cavity is coupled to two individual bosonic thermal baths with local dissipations. Consequently, the total Hamiltonian $\hat{H}_{\rm tot}$ under the mean-field approximation can be expressed as

$$\hat{H}_{\rm tot}=\hat{H}^s_{\rm MF}+\hat{H}_B+\hat{V}. \tag{8}$$

Here, the Hamiltonian of the thermal baths $\hat{H}_B$ is expressed as

$$\hat{H}_B=\sum_{u=q,c}\sum_k\omega_k\hat{b}^\dagger_{u,k}\hat{b}_{u,k}, \tag{9}$$

where $\hat{b}^\dagger_{u,k}$ ($\hat{b}_{u,k}$) creates (annihilates) one phonon in the uth bath with the frequency ω_k, $u=q$ refers to the qubit (atomic) bath and $u=c$ to the cavity (photonic) bath. The interactions between the Dicke system with thermal baths $\hat{V}$ is specified as

$$\hat{V}=\hat{V}_c+\hat{V}_q, \tag{10}$$

with

$$\hat{V}_q=\sum_k(\lambda_{q,k}\hat{b}^\dagger_{q,k}+\lambda^*_{q,k}\hat{b}_{q,k})(\hat{J}_++\hat{J}_-)/\sqrt{N}, \tag{11}$$

$$\hat{V}_c=\sum_k(\lambda_{c,k}\hat{b}^\dagger_{c,k}+\lambda^*_{c,k}\hat{b}_{c,k})(\hat{a}^\dagger+\hat{a}), \tag{12}$$

where $\lambda_{q,k}$ ($\lambda_{c,k}$) is the coupling strength between the atoms (photons) and the corresponding bath. The uth thermal bath is characterized by the spectral function $f_{q(c)}(\omega)=2\pi\sum_k|\lambda_{q(c),k}|^2\delta(\omega-\omega_k)$. In this paper, we specify $f_{q(c)}(\omega)$ the Ohmic case to quantify the thermal bath, i.e., $f_q(\omega)=\gamma_q\omega/\Delta\exp(-\omega/\omega_{\rm co})$, $f_c(\omega)=\gamma_c\omega/\omega_0\exp(-\omega/\omega_{\rm co})$, where $\gamma_{q(c)}$ is the dissipation strength and $\omega_{\rm co}$ is the cutoff frequency of thermal baths. $\omega_{\rm co}$ is considered to be large enough, so the spectral functions are simplified as $f_q(\omega)=\gamma_q\omega/\Delta$, $f_c(\omega)=\gamma_c\omega/\omega_0$.

We consider the case where the interaction between the DHM and thermal baths is weak. Under the Born-Markov approximation, the quantum DME used for investigating the dissipative dynamics of the density matrix is given by [76–80]

$$\frac{d}{dt}\hat{\rho}_s=-i\big[\hat{H}^s_{\rm MF},\hat{\rho}_s\big]+\sum_{u;m<n}\Big\{\Gamma^{nm}_u n_u(\Delta_{nm})\mathcal{D}[|\phi_n\rangle\langle\phi_m|,\hat{\rho}_s]+\Gamma^{nm}_u[1+n_u(\Delta_{nm})]\mathcal{D}[|\phi_m\rangle\langle\phi_n|,\hat{\rho}_s]\Big\}, \tag{13}$$

where $|\phi_m\rangle$ is the eigenfunction of the DHM under mean-field theory $\hat{H}^s_{\rm MF}$ as $\hat{H}^s_{\rm MF}|\phi_m\rangle=E_m|\phi_m\rangle$, $\Delta_{nm}=E_n-E_m$ is the transition frequency of two energy levels, the dissipator is

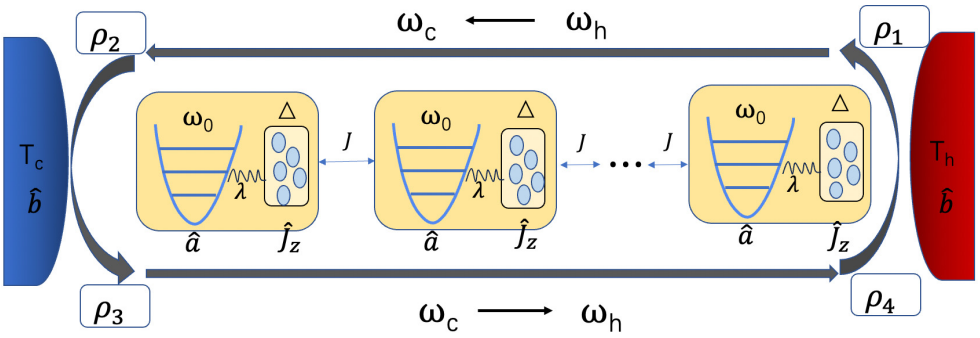


FIG. 1. Schematic representation of the four strokes of an Otto cycle for the realization of a heat machine based on the dissipative DHM. During the isochoric stroke the frequency of the working substance is held fixed while interacting with a hot (cold) reservoir at temperature T_h (T_c). Only heat is exchanged during this stroke. In the two quantum adiabatic strokes the working substance is isolated from the reservoir and has its frequency shifted, thus producing work. No heat is exchanged during this stroke. By controlling the parameters ω_0, Δ, J, and λ of the model, the machine can work as a heat engine, refrigerator, heater, or accelerator.

$\mathcal{D}[\hat{O},\hat{\rho}_s]=\frac{1}{2}[2\hat{O}\hat{\rho}_s\hat{O}^\dagger-\hat{\rho}_s\hat{O}^\dagger\hat{O}-\hat{O}^\dagger\hat{O}\hat{\rho}_s]$, the dissipative rates are $\Gamma_u^{jk}=f_u(\Delta_{nm})|S_u^{nm}|^2=\frac{\gamma_u\Delta_{nm}}{\omega_u}|S_u^{nm}|^2$, with $\omega_c=\omega_0$, $\omega_q=\Delta$, $S_q^{nm}=\frac{1}{\sqrt{N}}\langle\phi_n|(\hat{J}_+ +\hat{J}_-)|\phi_m\rangle$, and $S_c^{nm}=\langle\phi_n|(\hat{a}^\dagger+\hat{a})|\phi_m\rangle$. The Bose-Einstein distribution $n_u(\Delta_{nm})=1/[\exp(\Delta_{nm}/T_u)-1]$ accounts for thermal effects, T_u is the temperature coupled with the environment.

In the eigenbasis, the dynamics of the population $P_k=\langle\phi_k|\hat{\rho}_s|\phi_k\rangle$ is given by

$$\frac{d}{dt}P_k=\sum_{u,k\neq m}\Gamma_u^{km}n_u(\Delta_{km})P_m-\sum_{u,k\neq m}\Gamma_u^{km}[1+n_u(\Delta_{km})]P_k, \tag{14}$$

where $\Gamma_u^{km}=-\Gamma_u^{mk}$.

The steady state of the DHM is obtained by self-consistently solving the quantum dressed master equation. The specific process is (1) given an arbitrary reasonable initial value to the order parameter and solve $\hat{H}^s_{\rm MF}$ for eigenstates and eigenvalues; (2) find a temporary steady state $\rho_{\rm ss}$ via the quantum dressed master equation; and (3) update the order parameter $\psi=\mathrm{Tr}\{\rho_{\rm ss}a\}$ for the next-step iteration. This procedure can be repeated until the converged steady state and order parameter are achieved. All physical quantities can be calculated by the steady state.

It is important to emphasize that, unlike the standard master equation, quantum DME is applicable to arbitrary coupling strengths [76–79]. Our choice is fundamentally motivated by the principles of open quantum systems and thermodynamic consistency. Unlike the local Lindblad master equation, which naively applies dissipators directly to the bare operators $\hat{a}$ and $\hat{J}_x$ ($\hat{J}_z$), the quantum DME operates in the energy eigenbasis of the mean-field Hamiltonian $\hat{H}^s_{\rm MF}$. By resolving the bath correlation functions at the distinct transition frequencies Δ_{nm}, the quantum DME rigorously satisfies the Kubo-Martin-Schwinger condition. This guarantees that, in the weak system-bath coupling limit, the steady-state populations converge asymptotically to the canonical Gibbs distribution.

III. QUANTUM OTTO CYCLE

We employ the DHM as the working substance to engineer the four-stroke quantum Otto cycle, which is composed of two adiabatic and two isochoric processes [4,81]. During the isochoric process, the substance interacts with a hot (cold) reservoir at temperature T_h (T_c), and the four-stroke quantum Otto cycle has been shown in Fig. 1. The four strokes are, respectively, as follows:

Quantum isochoric process. The working substance as modeled by the mean-field Dicke Hamiltonian $H^s_{{\rm MF},h}$ with frequency $\omega=\omega_h$ ($\omega=\omega_0=\Delta$) is brought into contact with a hot reservoir at

temperature T_h. In this process, the system undergoes a Markovian evolution, which is described by Eq. (13).

After a long enough evolution, the system will reach the only steady state $\rho_1 = \rho_{\rm ss}(T_h) = \sum_n P_n^{\rm ss}(T_h)|E_n^h\rangle\langle E_n^h|$ with $\frac{d\rho}{dt} = 0$, where $P_n^{\rm ss}(T_h)$ is the corresponding population contact with hot reservoir at temperature T_h. The eigenstates $|E_n^h\rangle$ and eigenvalues E_n^h of $H_{{\rm MF},h}^s$ are obtained by using the extended bosonic coherent state approach method [74] with frequency $\omega = \omega_h$. During this process, heat Q_h is absorbed from the hot reservoir, without any work being done.

Quantum adiabatic expansion process. The system is isolated from the hot reservoir and the energy levels are changed from E_n^h to E_n^c by varying the frequency from ω_h to ω_c (with $\omega_h > \omega_c$). This process must be done slow enough to ensure that the populations $P_n^{\rm ss}$ (T_h) remain unchanged according to the quantum adiabatic theorem. At the end of this adiabatic expansion, the state becomes $\rho_2 = \sum_n P_n^{\rm ss}(T_h)|E_n^c\rangle\langle E_n^c|$. The eigenstates $|E_n^c\rangle$ and eigenvalues E_n^c of $H_{{\rm MF},c}^s$ are obtained by using the extended bosonic coherent state approach method with frequency $\omega = \omega_c$. During this process, only work is performed, with no heat being exchanged.

Quantum isochoric process. The working substance with frequency $\omega = \omega_c$ and modeled by the Hamiltonian $H_{Mf,c}^s$ is now put into contact with a cold reservoir at temperature $T_c < T_h$ until they reach thermal equilibrium. In this case, we have a change in the steady-state population from $P_n^{\rm ss}(T_h)$ to $P_n^{\rm ss}(T_c)$ ($P_n^{\rm ss}(T_c)$ is the corresponding population contact with cold reservoir at temperature T_c), while the eigenvalues E_n^c of the system remain unchanged, and the state becomes $\rho_3 = \sum_n P_n^{\rm ss}(T_c)|E_n^c\rangle\langle E_n^c|$. During this process, only heat is exchanged; heat Q_c is released to the cold reservoir, but no work is done.

Quantum adiabatic compression process. The system is isolated from the cold reservoir and its energy levels are changed back from E_n^c to E_n^h by varying the frequency from ω_c to ω_h. At the end of the process, the populations $P_n^{\rm ss}$ (T_c) remain unchanged, the state becomes $\rho_4 = \sum_n P_n^{\rm ss}(T_c)|E_n^h\rangle\langle E_n^h|$, and only work is performed by the working substance, but no heat is exchanged.

Next, let us calculate the work and heat exchanged in each stroke. According to the first law of thermodynamics, a quantum system with discrete energy levels can be written as

$$dU = \delta Q + \delta W = \sum_n \left(E_n dP_n^{\rm ss} + P_n^{\rm ss} dE_n\right), \tag{15}$$

where E_n are the energy levels of $\hat{H}_{\rm MF}^s$ and $P_n^{\rm ss}$ are the populations at steady state. Accordingly, the heat Q_h (Q_c) exchanges with the hot (cold) reservoir, and the net work W satisfies the following relations (more details are presented in Appendix C) [82]:

$$Q_h = \sum_n E_n^h \left[P_n^{\rm ss}(T_h) - P_n^{\rm ss}(T_c)\right], \tag{16}$$

$$Q_c = \sum_n E_n^c \left[P_n^{\rm ss}(T_c) - P_n^{\rm ss}(T_h)\right], \tag{17}$$

$$W = Q_h + Q_c = \sum_n \left(E_n^h - E_n^c\right)\left[P_n^{\rm ss}(T_h) - P_n^{\rm ss}(T_c)\right]. \tag{18}$$

It is worth emphasizing the convention adopted here for the mean-field order parameter. In our construction, the energy levels at corners 1 and 4 are those of the isochoric process in contact with the hot reservoir, $H_{\rm MF}^s(w_h;\psi_h)$, and those at corners 2 and 3 are those of the isochoric process in contact with the cold reservoir, $H_{\rm MF}^s(w_c;\psi_c)$, where $\psi_h(\psi_c)$ is the self-consistent order parameter of the hot (cold) steady state. Here, since the corner states are diagonal in the eigenbasis of these Hamiltonians, one has $U_k = {\rm Tr}(\rho_k H_{\rm MF}, k) = \sum_n P_n^{(k)} E_n^{(k)}$; consequently, Eqs. (16) and (17) are exactly the direct internal-energy differences $Q_h = U_1 - U_4$ and $Q_c = U_3 - U_2$, as shown explicitly in Appendix C. As in any ideal Otto cycle, the states at the corners 2 and 4 are nonequilibrium states whose populations are frozen from the preceding process, and ψ enters only through the energy levels of the isochoric processes.

TABLE I. Classification of working modes.

Working regimes	Q_h	Q_c	W
Heat engine (E)	>0	<0	>0
Refrigerator (R)	<0	>0	<0
Heater (H)	<0	<0	<0
Accelerator (A)	>0	<0	<0

In the following calculations, we will adopt the following convention: $Q > 0$ ($Q < 0$) correspond to absorption (release) of heat from (to) the reservoir while $W > 0$ ($W < 0$) correspond to work performed by (on) the quantum heat cycle. There are only four working regimes allowed under not violating the Clausius inequality with the first law of thermodynamics [83] as summarized in Table I.

In addition, we will study the performances of quantum Otto heat engine and refrigerator, where the performance of the heat engine is characterized by efficiency (marked by η), and its definition is $\eta = \frac{W}{Q_h}$; the performance of the refrigerator is characterized by the coefficient of performance (COP, marked by ξ), which is defined as $\xi = \frac{Q_c}{|W|}$.

IV. RESULTS AND DISCUSSIONS

First, we study the relationship between the superradiance phase transition and working mode of the quantum Otto cycle. We have known that at zero temperature, the steady state of the system will undergo a superradiant phase transition. In fact, such phase transition can occur at finite temperatures as well. Figures 2(a) and 2(b) show the steady state $|\psi|$ as functions of atom-light coupling strength λ and intercavity hopping strength under temperatures $T_c = 0.1$ and $T_h = 0.4$, respectively. The dark blue regions denote the normal phase while others denote the superradiance phase. When $T_c = 0.1$, it is seen that the superradiance phase covers a wide range of parameters, which indicates that the system is prone to superradiance phase transition at low temperatures. For the $T_h = 0.4$ case, the normal phase significantly expands, and only in the region with large λ and moderate J does the superradiance phase exist.

By comparing the results in Figs. 2(a) and 2(b), we can draw a common rule: When λ is relatively small, regardless of whether the system is exposed to a low-temperature heat source or a high-temperature heat source, the steady state remains in the normal phase. When λ is relatively large, regardless of whether the system is exposed to a low-temperature heat source or a high-temperature heat source, the steady state remains in the superradiance phase. Recent research has found that when the working substance is at the verge of the second-order quantum phase transition point, highly efficient quantum Otto heat engines can be achieved [6]. Inspired by this, a question emerges: If, in an Otto cycle, the steady states of the systems in contact with high- and low-temperature heat sources are all in the same quantum phase, would this synergistic mechanism be conducive to the realization of the heat engine? Here, the phrase "synergistic mechanism" refers to the situation where both hot and cold steady states lie in the same quantum phase. To answer this question, we take $T_c = 0.1$ and $T_h = 0.4$ to calculate the working mode of the quantum Otto cycle, and the results are presented in Fig. 2(c). It can be seen that the working area of the heat engine completely covers the regions of the normal phase and the superradiance phase. This indicates that the synergistic effect of the low-temperature heat source and the high-temperature heat source helps the Otto cycle to achieve the heat engine function. In addition, it can be observed that the competition effect between low-temperature heat sources and high-temperature heat sources, i.e., the different steady-state properties at high and low temperatures, will give rise to a rich variety of working modes, including the refrigerator, heater, accelerator, and heat engine. We have known that both the synergistic mechanism and the competitive mechanism can trigger the heat engine. Here, the phrase "competitive mechanism" refers to the case where they belong to different phases.

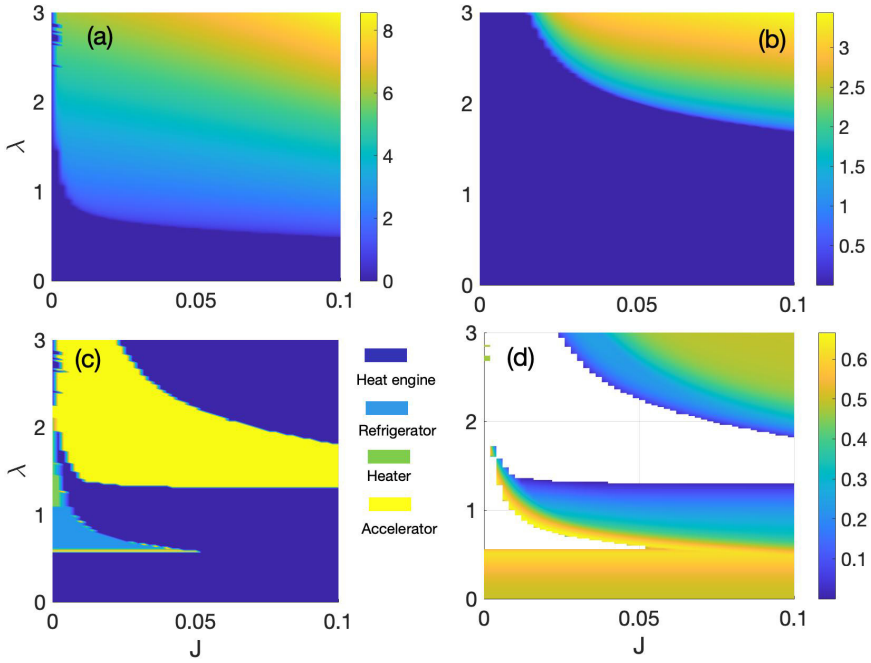


FIG. 2. (a), (b) The steady-state order parameter $|\psi|$ in λ-J parameter space under temperature $T_c = 0.1$ and $T_h = 0.4$. (c) Phase diagrams of the working modes of quantum Otto cycle in the λ-J parameter space with $T_c = 0.1$ and $T_h = 0.4$. (d) The efficiency of the quantum Otto heat engine. The other parameters are $N = 4$, $\omega_h = 2\omega$, $\omega_c = \omega$, and $\gamma_c = \gamma_q = 10^{-4}$.

Then, under which mechanism is the working efficiency of heat engine higher? Regarding this issue, we calculate the efficiency of the heat engine, and the results are presented in Fig. 2(d). It can be seen that the high efficiency is mainly distributed in the area under the synergistic mechanism. In particular, when the steady states at both low and high temperatures remain in the normal phase, the efficiency is higher. This result tells us that if one wants the heat engine to work at high efficiency, preparing the working substance in the normal phase is a much better choice.

Further, we study the influence of different heat source temperatures and atom-light coupling strengths on the working mode of the quantum Otto cycle. Figure 3 shows the variation of the working mode of the quantum Otto heat engine with the temperature T_h of the high-temperature heat source and the atom-light coupling strength λ under different low-temperature heat source temperatures T_c. Different colors represent different working modes: dark blue is the heat engine mode, light blue is the refrigerator mode, grass green is the heater mode, and yellow is the accelerator mode.

From Fig. 3(a), we can see that the heat engine mode occupies most of the area with a relatively small λ, indicating that when T_c is extremely low, the heat engine mode is easy to implement under weak-coupling condition. The region of the refrigerator mode is narrow, existing only when λ is small and T_h is within a specific range, and its application scope is limited. As λ increases, the system quickly enters the accelerator mode, indicating that under strong coupling, the Otto cycle is more inclined to the accelerator function. Compared with the result of $T_c = 0.1$, the mode distribution of $T_c = 0.2$ has changed significantly. As shown in Fig. 3(b), the mode range of the refrigerator mode has been significantly expanded, performing outstandingly within the range of moderate λ and moderate T_h. Moreover, the area of the heater mode gets larger. The heat engine mode still dominates in the smaller area of λ, but its relative proportion has slightly declined. The range of the accelerator mode in the larger area of λ is wider than the result in Fig. 3(a). For a slightly larger T_c case, it is

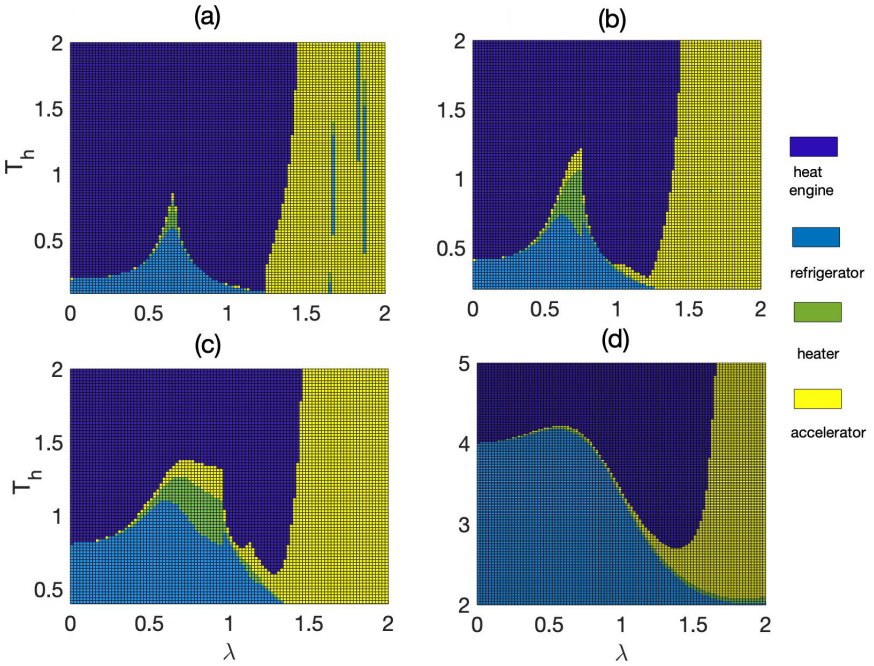


FIG. 3. Phase diagrams of the working modes of quantum Otto cycle in the T_h-λ parameter space under different T_c. (a) $T_c = 0.1$, (b) $T_c = 0.2$, (c) $T_c = 0.4$, and (d) $T_c = 2$. The color code stands for heat engine (dark blue), refrigerator (light blue), heater (grass green), and accelerator (yellow). The other involved parameters are $N = 8$, $J = 0.01$, $\omega_h = 2\omega$, $\omega_c = \omega$, and $\gamma_c = \gamma_q = 10^{-4}$.

seen from Fig. 3(c) that the regions of the refrigerator, heater, and accelerator modes further expand, while the working area of the heat engine is further compressed. For higher T_c, it can be seen from Fig. 3(d) that the region of the refrigerator mode has significantly expanded, becoming one of the core modes at this temperature. The region of the heat engine mode has narrowed, concentrating in the regions with higher T_h, and it almost disappears under strong coupling as well. Although the heat engine, heater, and accelerator modes still exist, the working area is significantly smaller compared to the results of $T_c = 0.2$ and $T_c = 0.4$, indicating that the higher T_c can suppress the three modes.

For different T_c, apart from causing differences in the distribution of working modes, they also bring some commonalities. For instance, the region λ with a relatively high coupling strength is mainly in the accelerator mode, indicating that strong coupling is the core trigger condition of the accelerator mode and has nothing to do with T_c. Moreover, the heat engine mode is always distributed within a relatively small λ and high T_h, indicating that relatively weak coupling and high-temperature heat source are fundamental conditions of the heat engine mode. The refrigerator mode is always distributed within a relatively small λ and low high T_h, indicating that relatively weak coupling and lower heat source temperature are fundamental conditions of the refrigerator mode. These results provide a reference for regulating the working mode of the quantum Otto cycle.

Furthermore, we analyze the efficiency of the quantum Otto heat engine. Figure 4 shows the working efficiency of the quantum Otto heat engine in the T_h-λ parameter space under different T_c values. The color changes from yellow to green and then to blue, indicating that the work efficiency decreases from high to low. Figure 4(a) shows the result of $T_c = 0.1$. It can be seen that the high work efficiency range covers a large area of $T_h \approx 0.5 \sim 2$ and $\lambda < 1$, and the efficiency is the highest at moderate λ. When $\lambda > 1$, the efficiency drops significantly, indicating that the strong atom-light coupling is not conducive to the operation of heat engine. Figure 4(b) shows the result of $T_c = 0.2$. Similar to the result of $T_c = 0.1$, the high efficiency is mainly concentrated in the interval

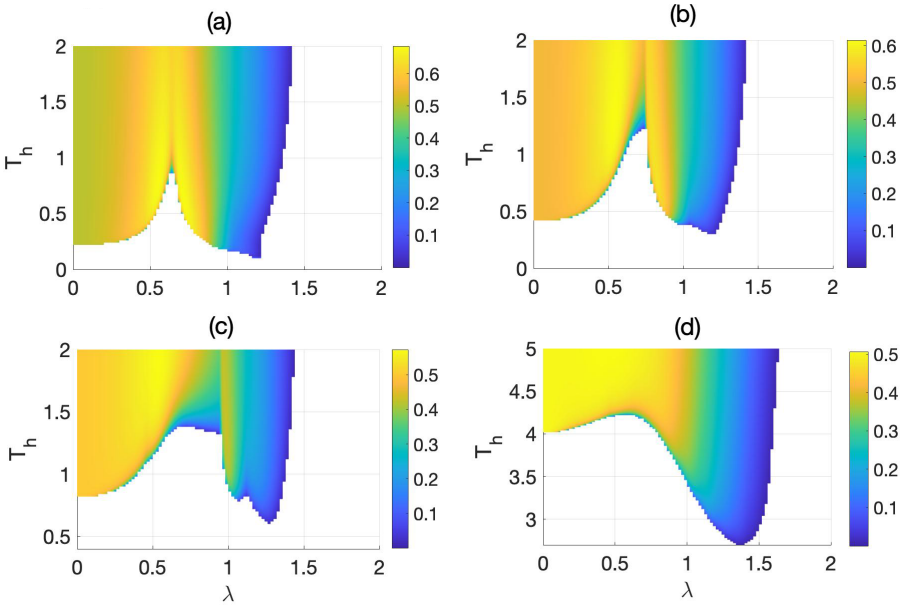


FIG. 4. The efficiency of the quantum Otto heat engine: (a) $T_c = 0.1$, (b) $T_c = 0.2$, (c) $T_c = 0.4$, and (d) $T_c = 2$. Other involved parameters are $N = 8$, $J = 0.01$, $\omega_h = 2\omega$, $\omega_c = \omega$, and $\gamma_c = \gamma_q = 10^{-4}$.

where $\lambda < 1$, and the efficiency is the highest when the value of λ is moderate. When the J gets stronger ($\lambda > 1$), the efficiency declines, signaling again that the strong coupling is not conducive to the operation of heat engine. For the $T_c = 0.4$ case, it is seen from Fig. 4(c) that the efficiency distribution characteristics are similar to those of $T_c = 0.1$ and $T_c = 0.2$. The high efficiency appears in the relatively weak-coupling region, and the strong coupling is not conducive to the realization of the high-efficiency heat engine. The result of $T_c = 2$ is presented in Fig. 4(d). It can be seen that the bright yellow interval moves up to $T_h \approx 4 \sim 5$, but it is also distributed in the weak-coupling region ($\lambda < 1$). When $\lambda > 1$, efficiency drops rapidly as well. Through the study of heat engine efficiency, it has been clarified that weak coupling ($\lambda < 1$) is the key to high efficiency, while strong coupling will lead to a decrease in efficiency. This result has guiding significance for the design of high-efficiency quantum Otto heat engines.

In addition, we investigate the influence of different intercavity hopping strengths on the superradiance phase transition at different temperatures, and compare the differences in output work and efficiency under different J. The results are presented in Figs. 5(a)–5(d), respectively. As can be seen from Fig. 5(a), the larger the J, the smaller the critical λ, indicating that the intercavity hopping strength J can promote superradiance at low temperature. However, the variation trend of the phase transition point is not very obvious as J further increases. Compared with the results in Fig. 5(a), the superradiance phase transition point at high temperatures also shows a similar trend of change, but the difference lies in that the superradiance phase transition point is more sensitive to the change of J. At the same time, it can be seen that at high temperatures, the nonzero regions of the order parameter $|\psi|$ corresponding to different J significantly decrease, further verifying the suppression effect of temperature on the superradiance phase transition. As can be seen from Fig. 5(c), under the weak intercavity hopping condition, such as $J = 0.01$, the heat engine has the maximum output work, while under the larger, such as $J = 0.1$, the peak output work is the lowest. However, if it is necessary for the heat engine to have good output work, it is essential to adjust λ and J within an appropriate range. Concretely, fixing λ in the weak atom-light coupling interval is a better choice. Figure 5(d) reflects the working efficiency of the heat engine, and the inset magnifies the details of the high-efficiency range. It can be seen that the peak of efficiency is not sensitive to the change of

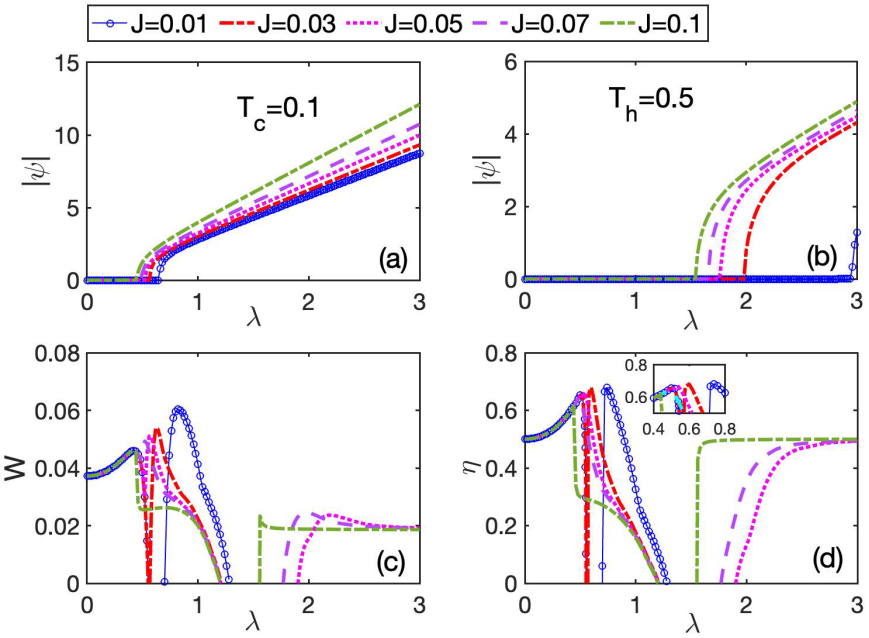


FIG. 5. (a), (b) The steady-state order parameter $|\psi|$ as the function of atom-light coupling strength λ under different hopping strength J. The temperature is taken as (a) $T_c = 0.1$ and (b) $T_h = 0.5$. (c), (d) The efficiency η and work W of the quantum heat engine as a function of the atom-light coupling strength λ for different hopping strength J, keeping $T_c = 0.1$ and $T_h = 0.5$. The other system parameters are given by $N = 8$, $\omega_h = 2\omega$, $\omega_c = \omega$, and $\gamma_c = \gamma_q = 10^{-4}$.

J. Adjusting λ and J within an appropriate range can enable the heat engine to operate with good performance. Concretely, to ensure that the output work of the heat engine is no less than 0.04, it is a better choice to set λ in the weak atom-light coupling region. When λ is set in the appropriate weak or strong atom-light coupling regions, the heat engine can achieve at least a 0.5 working efficiency.

We also investigate the influence of different atomic numbers N on the superradiance phase transition, output work, and efficiency, and the results are presented in Figs. 6(a)–6(d), respectively. As can be seen from Figs. 6(a) and 6(b), the more N is, the smaller the critical λ of the phase transition becomes, indicating that a greater number of atoms can promote superradiance phase transitions. However, through comparison, it is found that the changing trend of the phase transition critical point at high temperatures is more obvious than that at low temperatures. As can be seen from Fig. 6(b), the superradiance phase transition will only occur when the number of atoms is large and the atom-light coupling strength is very strong. Here, the suppression effect of temperature on the superradiative phase transition is verified. As can be seen from Fig. 6(c), the output work of the heat engine depends on the coordinated regulation of λ and N. When N is smaller, the peak value of the output work is higher. Besides, we can see that regardless of whether the atom-light coupling strength is weak or strong, the appropriate atomic number conditions can always be found to keep the output work no less than 0.04. The phenomena are slightly different from those under different J conditions. In Fig. 6(d), we can see that no matter it is the strong atom-light coupling or the weak coupling, the appropriate atomic number conditions can always be found, which enables the heat engine to have a good performance with a working efficiency no less than 0.5.

For our analysis, we recall the analytical results: $\eta_{\lambda=0} = 1 - \omega_c/\omega_h$ for efficiency and $\xi_{\lambda=0} = \omega_c/(\omega_h - \omega_c)$ for COP of an Otto cycle when $\lambda = 0$, which corresponds to N qubits and a noninteracting bosonic mode. As observed from Figs. 4–6, for a broad range of couplings, η surpasses the quantum Otto efficiency of a working medium with a harmonic spectrum $\eta_{\lambda=0} = 1 - \omega_c/\omega_h = 0.5$.

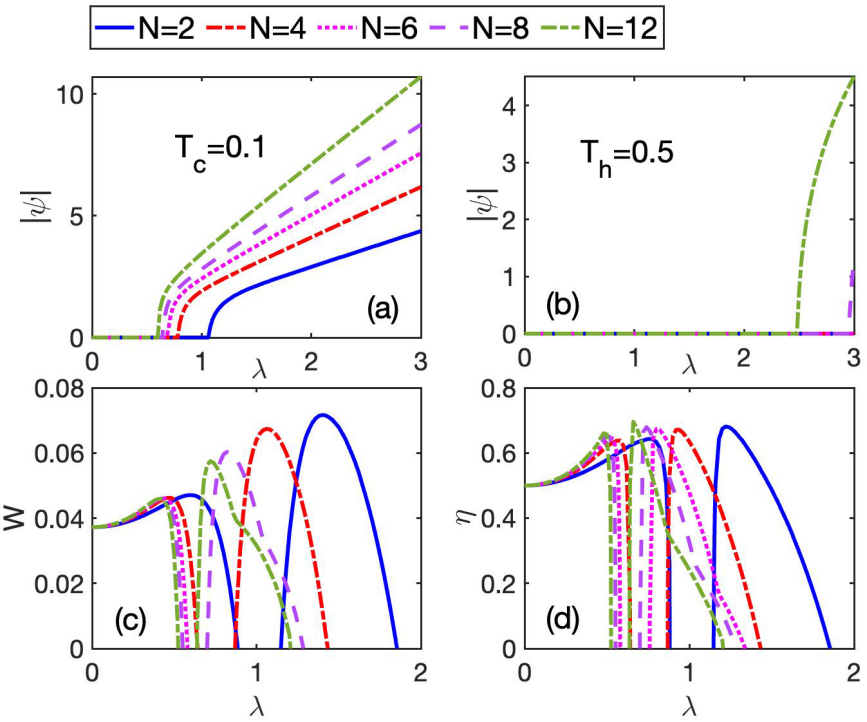


FIG. 6. (a), (b) The steady-state order parameter $|\psi|$ as the function of qubit-boson coupling strength λ under different qubit numbers with fixed hopping strength $J = 0.01$. The temperature is taken as (a) $T_c = 0.1$ and (b) $T_h = 0.5$. (c), (d) The efficiency η and work W of the quantum heat engine as a function of the qubit-boson coupling strength λ for different qubit numbers with fixed hopping strength $J = 0.01$, $T_c = 0.1$, and $T_h = 0.5$. The other parameters are $\omega_h = 2\omega$, $\omega_c = \omega$, and $\gamma_c = \gamma_q = 10^{-4}$.

The results above are all based on the case of resonance. Now, we will investigate how detuning $\delta = \Delta - \omega$ between the frequency Δ of each of the N qubits and the frequency ω of the field mode in the cavity affects the efficiency of DHM. Figure 7 shows the efficiency for several values of δ; the figure indicates that as δ increases, the efficiency value can surpass the resonance case, $\delta = 0$, and even approach the Carnot limit $\eta_{\text{Carnot}} = 1 - T_c/T_h = 0.8$ marked by the horizontal gray solid line.

From some figures, we can clearly see some discontinuous jumps. Taking $J = 0.01$ as an example for analysis, other discontinuous jumps can be analyzed in the same way. These jumps are most evidently reflected in Fig. 8(b), which presents the output work W, the heat absorbed from the hot bath Q_h, and the heat released to the cold bath Q_c as functions of the atom-light coupling strength λ. Taking the specific point $\lambda \approx 0.55$ as an illustration, one can observe that both W and Q_h undergo abrupt changes across this value, and consequently the efficiency $\eta = W/Q_h$ exhibits a sharp discontinuous jump. This critical λ marks the superradiant phase transition of the dissipative Dicke-Hubbard model: As λ crosses the transition point, the steady-state energy spectrum and population distribution of the working substance change suddenly, causing simultaneous discontinuities in Q_h, Q_c, and hence in $W = Q_h + Q_c$ (with $Q_c < 0$). The background color coding in Fig. 8(b) further confirms that this jump coincides with the boundary between different operating modes (heat engine, refrigerator, heater, and accelerator), indicating that the phase transition directly dictates the abrupt change in the thermodynamic performance. Similar jumps occurring at other critical values of λ can be attributed to the same physical mechanism.

To verify the thermodynamic consistency of the quantum Otto cycle, we evaluate the total entropy production per cycle [3,84,85], $\Delta S_{\text{tot}} = -Q_h/T_h - Q_c/T_c$. Figure 9 presents ΔS_{tot} as a function of

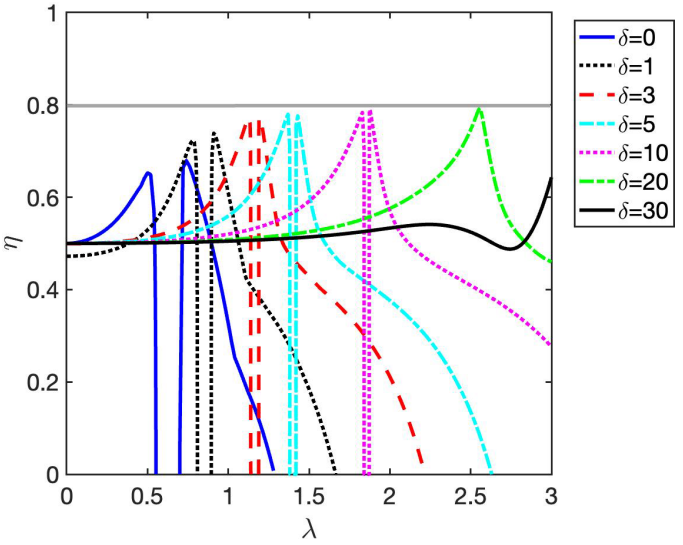


FIG. 7. The efficiency η of the quantum heat engine as a function of the qubit-boson coupling strength λ for different detuning $\delta = \Delta - \omega$ between the frequency ω of the field mode in the cavity and the frequency Δ of each of the N atoms with fixed hopping strength $J = 0.01$, $T_c = 0.1$, and $T_h = 0.5$. The other parameters are $\gamma_c = \gamma_q = 10^{-4}$.

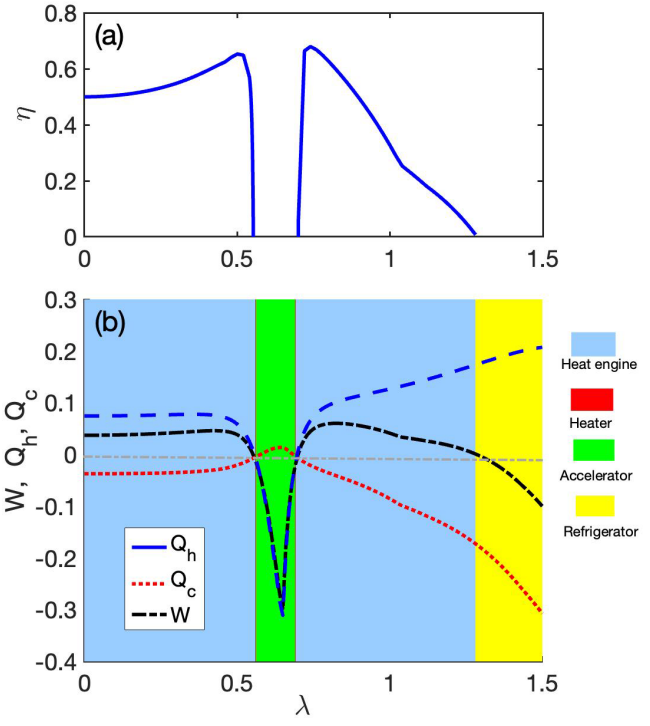


FIG. 8. (a), (b) Efficiency, work output, and heat as functions of the qubit-boson coupling strength λ with fixed hopping strength $J = 0.01$. The background color coding represents different operating modes: heat engine (blue), refrigerator (green), heater (yellow), and accelerator (red). The other parameters are $\omega_h = 2\omega$, $\omega_c = \omega$, $T_c = 0.1$, $T_h = 0.5$, and $\gamma_c = \gamma_q = 10^{-4}$.

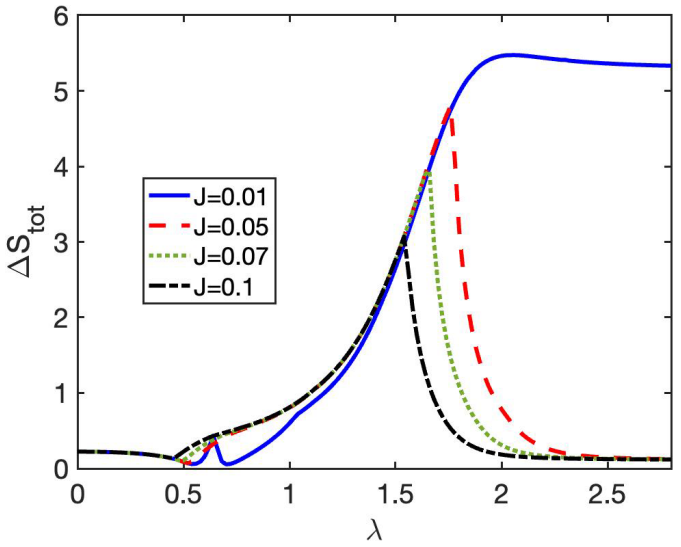


FIG. 9. The total entropy production per cycle as functions of the qubit-boson coupling strength λ under different hopping strength J. The other parameters are $N = 8$, $\omega_h = 2\omega$, $\omega_c = \omega$, $T_c = 0.1$, $T_h = 0.5$, and $\gamma_c = \gamma_q = 10^{-4}$.

the atom-light coupling strength λ for different intercavity hopping strengths. For all values of J, ΔS_{tot} is strictly non-negative across the entire parameter range, confirming that our dressed-master-equation treatment yields thermodynamically consistent steady states. It confirms that our quantum Otto cycle respects the second law of thermodynamics in all parameter regimes. Interestingly, for small λ (the normal-phase regime), ΔS_{tot} decreases monotonically from its maximum at $\lambda = 0$ to a minimum near $\lambda = 0.5$. This indicates that the cycle operates closer to the reversible limit in the weak-coupling normal phase, consistent with our earlier observation that high heat engine efficiency is achieved in this regime. For intermediate coupling strengths, the behavior of ΔS_{tot} depends sensitively on J; in the strong-coupling regime ($\lambda \geqslant 1.0$), ΔS_{tot} initially grows with λ reaching a maximum before decreasing. And for all J, ΔS_{tot} tends to a finite asymptotic value as $\lambda \to \infty$, indicating that even in the deep strong-coupling limit, the cycle retains a finite level of irreversibility.

V. COMPARISON BETWEEN DHM AND DM

The DM, as a representative model for describing the collective interaction between light and matter, is widely used as the working medium of the quantum Otto cycle due to its unique collective coupling effect and quantum phase transition characteristics, laying the foundation for studying the core performance indicators such as output work and efficiency of quantum thermal devices under collective interaction. The DHM, on the basis of the collective light-matter interaction of the DM, introduces the local Hubbard interaction between light fields. The addition of this interaction changes the collective excitation behavior of the system, resulting in significant differences in heat exchange and work transfer during the thermodynamic process of the quantum Otto cycle using it as the working medium compared with the traditional DM.

We first discuss the differences between the DM and the DHM in terms of their collective excitation behaviors. Figure 10(a) shows the steady-state photon excitation number of the DM at a high temperature $T_h = 0.5$. It can be seen that the photon excitation number increases gradually with the rise of the atom number. For the DHM at the same temperature, we observe a distinct variation behavior. As shown in Fig. 10(b), the photon excitation number first decreases and

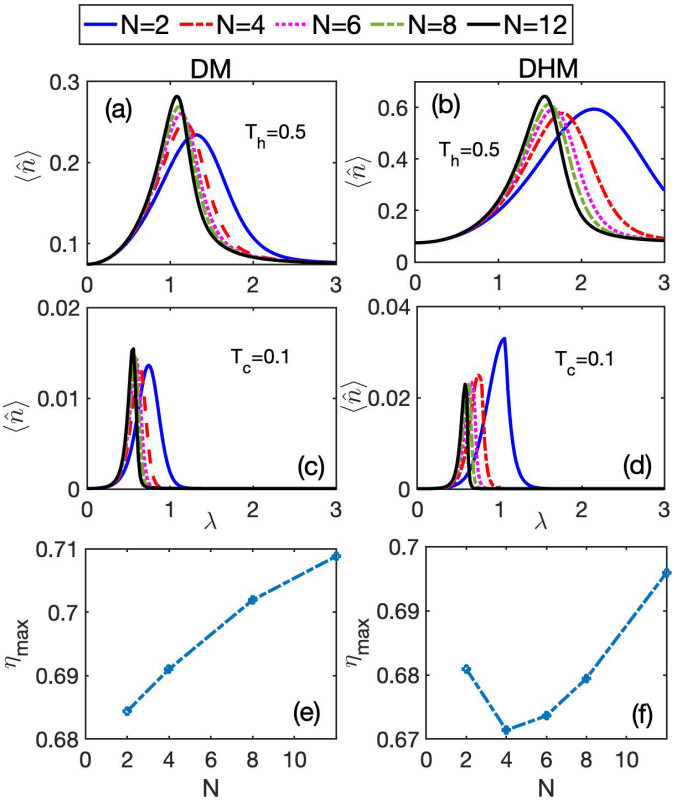


FIG. 10. (a), (b) The steady-state average photon excitation number for DM and DHM with $T_h = 0.5$, respectively. (c), (d) The steady-state average photon excitation number for DM and DHM with $T_c = 0.1$, respectively. (e), (f) The maximum efficiency $\eta_{\max}$ as a function of the qubit-boson coupling strength λ for different qubit numbers N. The involved parameters are $J = 0.01$, $T_c = 0.1$, $T_h = 0.5$, $\omega_h = 2\omega$, $\omega_c = \omega$, and $\gamma_c = \gamma_q = 10^{-4}$.

then increases with an increasing atom number. For the low-temperature case with $T_c = 0.1$, the excitation behaviors of the two models also exhibit discrepancies. From Fig. 10(c), it is found that the variation behavior of the atomic excitation number with the atom number is consistent with that at high temperature, also increasing gradually until saturation; for the DHM, however, the variation trend of the photon excitation number with the atom number differs from that in its low-temperature case. As illustrated in Fig. 10(d), the photon excitation number decreases gradually with the increase of the atom number until saturation. Through comparison, the photon excitation number at high temperature is obviously larger than that at low temperature, which indicates that temperature exerts a significant influence on the steady-state photon excitation number. By the rational control of temperature, the photon excitation and blockade of the DM and DHM can be realized.

The discrepancies in collective excitation behaviors between DM and DHM lead to distinct performance of the Otto heat engine when the two models are employed as the working medium. In Figs. 10(e) and 10(f), we plot the variation of the maximum working efficiency $\eta_{\max}$ of the Otto heat engine with the atom number N for DM and DHM as the working medium, respectively. As shown in Fig. 10(e), $\eta_{\max}$ of the Otto heat engine with DM as the medium increases with the rise of N. Figure 10(f) demonstrates that $\eta_{\max}$ of the Otto heat engine with DHM as the medium first decreases and then increases as N increases. In addition, we calculate the variation of the output

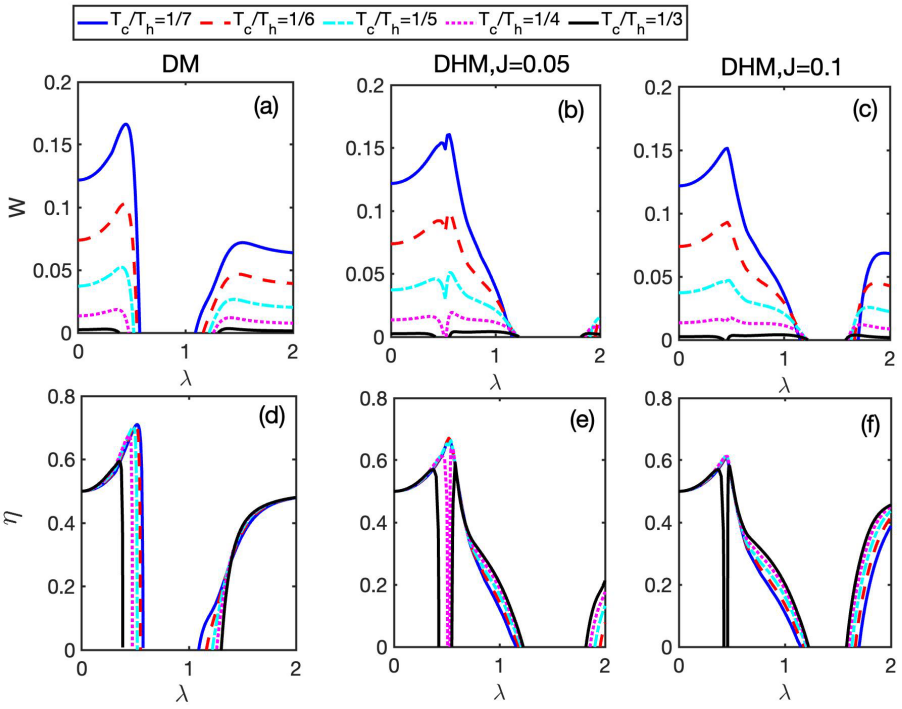


FIG. 11. Comparing the output work and efficiency of DHM and DM as a function of the qubit-boson coupling strength λ at different temperature ratios. The other parameters are $\omega_h = 2\omega$, $\omega_c = \omega$, and $\gamma_c = \gamma_q = 10^{-4}$.

work and efficiency of the Otto cycle with the atom-light coupling strength λ for the two working media at different temperatures, with the results presented in Figs. 11(a)–11(f). A comparison of Figs. 11(a) and 11(b), as well as Figs. 11(d) and 11(e), reveals that the DHM exhibits no obvious advantages in terms of output work and heat engine efficiency, with its peak values lower than those of the DM. With a further increase in the atom-light coupling strength, as seen in Figs. 11(e) and 11(f), the DHM shows a more pronounced disadvantage, with its peak values of output work and efficiency decreasing significantly further. This indicates that the DM is more suitable than the DHM for the design of high-performance Otto heat engine.

Given that the DM exhibits a distinct performance advantage over the DHM in Otto heat engines, it becomes a question worthy of further investigation whether the two models follow a similar trend in their performance for refrigerator applications. Based on this, we take the quantum Otto refrigerator as the research framework in the following and systematically compare the key performance metric of the refrigerator—the COP—when the DM and DHM are employed as the working medium, respectively. Figure 12(a) shows the COP (denoted by ξ) as a function of λ for the DHM as the working medium with $J = 0.05$ and varying T_h. Figure 12(b) presents the same quantity ξ versus λ for the DHM under $J = 0.1$ and different T_h. Figure 12(c) displays ξ as a function of λ for the DM as the working medium with $J = 0.1$ and varying T_h. A comparison of the COP results shown in these three panels reveals that the COP of the Otto refrigerator with the DHM as the working medium is significantly higher than that with the DM. This demonstrates that the DHM with multicavity coupling is more suitable than the single-cavity DM for the design of high-performance quantum Otto refrigerator. In addition, a comparison of the results in Figs. 12(a) and 12(b) shows that the COP increases with an increase in J in the regime of stronger atom-light coupling, which

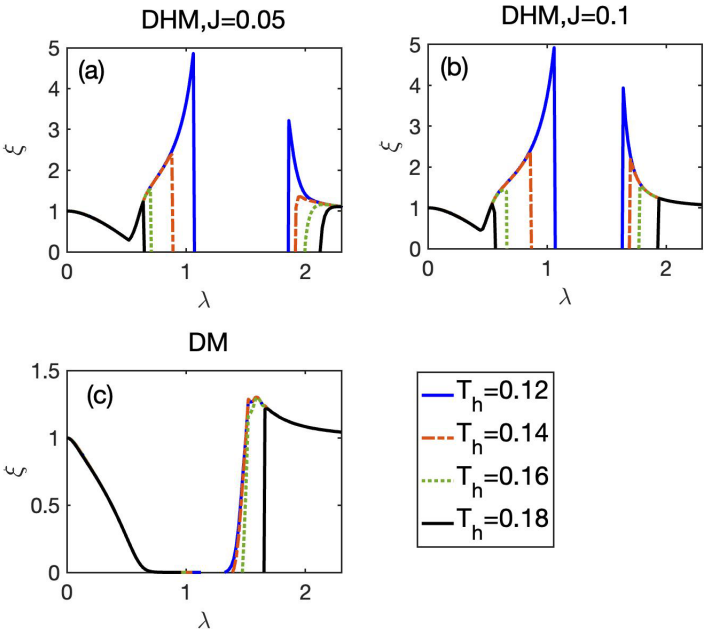


FIG. 12. Comparing the COP of DHM and DM as a function of the qubit-boson coupling strength λ at different temperature T_h with fix $T_c = 0.1$. The other parameters are $\omega_h = 2\omega$, $\omega_c = \omega$, and $\gamma_c = \gamma_q = 10^{-4}$.

indicates that enhanced intercavity coupling can further optimize the overall performance of the quantum Otto refrigerator.

In addition, as observed in Fig. 12, it shows that the Otto COP $\xi_{\lambda=0} = \omega_c/(\omega_h - \omega_c) = 1$ when $\lambda = 0$, and as λ increases, the Dicke model as a working substance surpasses that of the decoupled system used to fuel the quantum refrigerator. However, within these parameter spaces, it remains less than the Carnot COP limit $\xi < \xi_{\text{Carnot}} = T_c/T_h - T_c$.

VI. SUMMARY

In conclusion, this paper has taken the dissipative Dicke-Hubbard model as the research object and constructs a quantum Otto cycle with the model as the working substance, to systematically explore the intrinsic relationship between superradiance phase transition and the performance of quantum heat engines and refrigerators. Using mean-field approximation, the extended bosonic coherent state approach, and the quantum dressed master equation, we analyze the regulation laws of parameters such as temperature, atom-light coupling strength, intercavity hopping strength, and atom number on the working mode, efficiency, and coefficient of performance of the cycle. The results show that the steady-state synergistic mechanism under high- and low-temperature environments facilitates high-performance quantum heat engines, while the competitive mechanism is more conducive to high-performance quantum refrigerators. High heat engine efficiency tends to be achieved in the weak-coupling and normal-phase regions, whereas strong coupling easily drives the system into the accelerator mode. Compared with the single-cavity Dicke model, the Dicke-Hubbard model presents no obvious advantages in output work and efficiency of heat engines, but its multicavity coupling structure significantly improves the coefficient of performance, making it more suitable for constructing high-efficiency quantum refrigerators. Moreover, enhancing intercavity hopping can further optimize refrigeration performance. In addition, intercavity hopping and atom number can promote superradiance phase transition, while temperature suppresses it. This study clarifies the energy conversion mechanism in nonequilibrium quantum thermodynamics, reveals the

application potential of many-body quantum systems in quantum heat engines and refrigerators, and provides solid theoretical support for the parameter optimization of high-performance quantum thermal devices.

In recent years, cavity quantum electrodynamics (cavity QED) and superconducting circuit QED have been widely recognized as ideal experimental platforms for realizing and simulating the Rabi-Hubbard model and the Dicke-Hubbard model. This system exhibits a series of prominent advantages: It can stably achieve strong and even ultrastrong light-matter coupling [86,87], features highly controllable and continuously tunable system parameters, can be conveniently extended to multisite lattice structures, allows precise introduction and regulation of dissipation and environmental coupling, and can be directly applied to construct and characterize quantum heat engines and quantum refrigerators. The rapid development and experimental breakthroughs of cavity QED and circuit QED have provided unprecedented experimental potential for observing, manipulating, and verifying superradiance quantum phase transitions in high-performance, highly controllable advanced quantum architectures. Furthermore, the above unique advantages can be further extended to more complex and strongly correlated coupled light-matter many-body systems, whose quantum dynamics and nonequilibrium behaviors often exceed the simulation capability of classical computers, offering an irreplaceable research approach for exploring many-body quantum thermodynamics and energy conversion mechanisms. It is expected that in the near future, the theoretical predictions we have made can be realized on these platforms.

ACKNOWLEDGMENTS

We thank G. D. M. Neto for helpful discussions and suggestions. S.C. acknowledges the support from the Natural Science Foundation of Zhejiang Province (Grant No. LQN25A040012) and the start-up fund from Xingzhi College, Zhejiang Normal University, and the National Natural Science Foundation of China under Grant No. 12604416. H.-G.X. acknowledges the support from Start-up Fund of the School of Physics and Optoelectronic Engineering, Guangdong Polytechnic Normal University, under Grant No. 2026SDKYA018.

DATA AVAILABILITY

There are no publicly available research data or software supporting this manuscript. Requests for further information or data should be sent to the authors.

APPENDIX A: DERIVATION OF THE EXTENDED BOSONIC COHERENT STATE

By considering the displacement transformation $\hat{A}_m = \hat{a} + g_m$, with $g_m = \frac{2\lambda m}{\omega_0\sqrt{N}} - \frac{zJ\psi}{\omega_0}$, the Schrödinger equation of $\hat{H}^s_{\mathrm{MF}}$ on the basis is given by

$$-\Delta j_m^+|\varphi_m\rangle_b|j,m+1\rangle - \Delta j_m^-|\varphi_m\rangle_b|j,m-1\rangle + \omega_0\big(\hat{A}_m^\dagger\hat{A}_m - g_m^2 + zJ\psi^2\big)|\varphi_m\rangle_b|j,m\rangle = E|\varphi_m\rangle_b|j,m\rangle, \tag{A1}$$

where $\hat{J}_\pm|j,m\rangle = j_m^\pm|j,m\pm1\rangle$, with $j_m^\pm = \frac{1}{2}\sqrt{j(j+1)-m(m\pm1)}$. Next, we multiply Eq. (A1) on the left by $\{\langle n,\, j|\}$, which results in

$$-\Delta j_n^+|\varphi_{n+1}\rangle_b - \Delta j_n^-|\varphi_{n-1}\rangle_b + \omega_0\big(\hat{A}_n^\dagger\hat{A}_n - g_n^2 + zJ\psi^2\big)|\varphi_n\rangle_b = E|\varphi_n\rangle_b, \tag{A2}$$

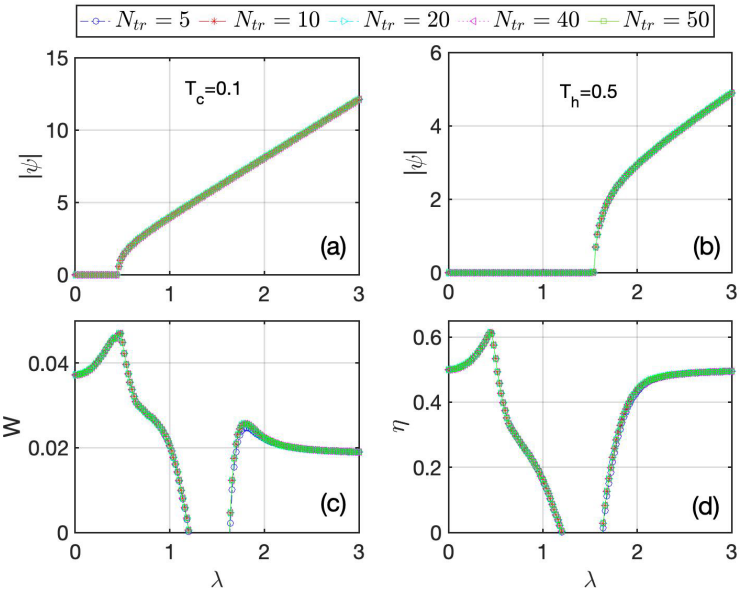


FIG. 13. (a), (b) Convergence check of the steady-state order parameter $|\psi|$ by increasing the truncation number of photons $N_{\rm th}$ as the function of qubit-boson coupling strength λ with fixed hopping strength $J = 0.1$. The temperature is taken as (a) $T_c = 0.1$ and (b) $T_h = 0.5$. (c), (d) The efficiency η and work W of the quantum heat engine by increasing the truncation number of photons $N_{\rm th}$ as a function of the qubit-boson coupling strength λ with fixed hopping strength $J = 0.1$, $T_c = 0.1$, and $T_h = 0.5$. The other parameters are $N = 8$, $\omega_h = 2\omega$, $\omega_c = \omega$, and $\gamma_c = \gamma_q = 10^{-4}$.

where $n = -j, -j+1, \ldots, j$. Furthermore, the bosonic state can be expanded as

$$|\varphi_m\rangle_b = \sum_{k=0}^{N_{\rm tr}} \frac{1}{\sqrt{k!}} c_{m,k} (\hat{A}_m^\dagger)^k |0\rangle_{A_m} = \sum_{k=0}^{N_{\rm tr}} \frac{1}{\sqrt{k!}} c_{m,k} (\hat{a}^\dagger + g_m)^k e^{-g_m \hat{a}^\dagger - g_m^2/2} |0\rangle_b, \tag{A3}$$

where $N_{\rm tr}$ is the truncation number of photonic excitations and $|0\rangle_b$ is vacuum state. Finally, we obtain the eigenvalue equation

$$\omega_0 \left(l - g_n^2 + zJ\psi^2\right) c_{n,l} - \Delta j_n^+ \sum_{k=0}^{N_{\rm tr}} c_{n+1,kA_n} \langle l|k\rangle_{A_{n+1}} - \Delta j_n^- \sum_{k=0}^{N_{\rm tr}} c_{n-1,kA_n} \langle l|k\rangle_{A_{n-1}} = E c_{n,l}, \tag{A4}$$

where the coefficients are ${}_{A_n}\langle l|k\rangle_{A_{n-1}} = (-1)^l D_{l,k}$ and ${}_{A_n}\langle l|k\rangle_{A_{n+1}} = (-1)^k D_{l,k}$, with (see Appendix B for details)

$$D_{l,k} = e^{-G^2/2} \sum_{r=0}^{\min[l,k]} \frac{(-1)^{-r} \sqrt{l!k!} G^{l+k-2r}}{(l-r)!(k-r)!r!}, \tag{A5}$$

where $G = \frac{2\lambda}{\omega_0 \sqrt{N}}$.

To ensure the numerical accuracy of our method of extended bosonic coherent state, we performed convergence tests. Figure 13 shows the convergence tests for several typical physical quantities calculated in this paper. From Fig. 13, we can know that we select the truncation number $N_{\rm tr} = 50$ up to $N = 8$, which is sufficient to guarantee the convergence of the steady-state order parameter $|\psi|$, efficiency η and work W as shown in Fig. 13.

APPENDIX B: DERIVATION OF ${}_{A_m}\langle l|k\rangle_{A_n}$

The detailed expression of ${}_{A_m}\langle l|k\rangle_{A_n}$, denoting the inner product of modified phonon states with effective displacements g_m and g_n, can be derived as follows:

$$
\begin{aligned}
{}_{A_m}\langle l|k\rangle_{A_n} &= e^{-(g_n^2+g_m^2)/2}{}_b\langle 0|e^{-g_m\hat{a}}\frac{(\hat{a}+g_m)^l}{\sqrt{l!}}\frac{(\hat{a}^\dagger+g_n)^k}{\sqrt{k!}}e^{-g_n\hat{a}^\dagger}|0\rangle_b \\
&= \frac{e^{-(g_n^2+g_m^2)/2}}{\sqrt{l!}\sqrt{k!}}{}_b\langle 0|e^{-g_m\hat{a}}(\hat{a}+g_m)^l(\hat{a}^\dagger+g_n)^k e^{-g_n\hat{a}^\dagger}|0\rangle_b \\
&= \frac{e^{-(g_n-g_m)^2/2}}{\sqrt{l!}\sqrt{k!}}{}_b\langle 0|(\hat{a}+g_m)^l e^{-g_n\hat{a}^\dagger}e^{-g_m\hat{a}}(\hat{a}^\dagger+g_n)^k|0\rangle_b \\
&= \frac{e^{-(g_n-g_m)^2/2}}{\sqrt{l!}\sqrt{k!}}{}_b\langle 0|(\hat{a}+g_m-g_n)^l(\hat{a}^\dagger+g_n-g_m)^k|0\rangle_b \\
&= \frac{e^{-(g_n-g_m)^2/2}}{\sqrt{l!}\sqrt{k!}}\sum_{r=0}^{\min\{l,k\}} r!C_l^r(g_m-g_n)^{l-r}C_k^r(g_n-g_m)^{k-r} = (-1)^k D_{l,k}(g_m-g_n),
\end{aligned}
$$

where

$$
D_{l,k} = e^{-G^2/2}\sum_{r=0}^{\min[l,k]}\frac{(-1)^{-r}\sqrt{l!k!}G^{l+k-2r}}{(l-r)!(k-r)!r!} \tag{B1}
$$

is invariant under the exchange of indices l, k.

APPENDIX C: EQUIVALENCE OF EQS. (16)–(18) WITH THE DIRECT INTERNAL-ENERGY DIFFERENCES

Let $\hat{H}_{\mathrm{MF},k}$ denote the mean-field Hamiltonian assigned to the kth corner in the Otto cycle, with $\hat{H}_{\mathrm{MF},1}=\hat{H}_{\mathrm{MF},4}=\hat{H}^s_{\mathrm{MF}}(\omega_h;\psi_h)$ and $\hat{H}_{\mathrm{MF},2}=\hat{H}_{\mathrm{MF},3}=\hat{H}^s_{\mathrm{MF}}(\omega_c;\psi_c)$. Writing the corner states as $\rho_k=\sum_n P_n^{(k)}|E_n^{(k)}\rangle\langle E_n^{(k)}|$ with $\hat{H}_{\mathrm{MF},k}|E_n^{(k)}\rangle = E_n^{(k)}|E_n^{(k)}\rangle$, the internal energies are $U_k=\mathrm{Tr}(\rho_k\hat{H}_{\mathrm{MF},k})=\sum_n P_n^{(k)}E_n^{(k)}$. Hence, we have

$$
\begin{aligned}
Q_h &= U_1-U_4=\sum_n E_n^h\big[P_n^{\mathrm{ss}}(T_h)-P_n^{\mathrm{ss}}(T_c)\big], \\
Q_c &= U_3-U_2=\sum_n E_n^c\big[P_n^{\mathrm{ss}}(T_c)-P_n^{\mathrm{ss}}(T_h)\big],
\end{aligned} \tag{C1}
$$

and $W=Q_h+Q_c$. The heat and work employed in this work are therefore identical to the internal-energy differences evaluated with the mean-field Hamiltonians of the cycle.

[1] S. Vinjanampathy and J. Anders, Quantum thermodynamics, Contemp. Phys. **57**, 545 (2016).
[2] J. Millen and A. Xuereb, Perspective on quantum thermodynamics, New J. Phys. **18**, 011002 (2016).
[3] R. Kosloff, Quantum thermodynamics: A dynamical viewpoint, Entropy **15**, 2100 (2013).
[4] H. T. Quan, Y. X. Liu, C. P. Sun, and F. Nori, Quantum thermodynamic cycles and quantum heat engines, Phys. Rev. E **76**, 031105 (2007).
[5] R. Uzdin, A. Levy, and R. Kosloff, Equivalence of quantum heat machines, and quantum-thermodynamic signatures, Phys. Rev. X **5**, 031044 (2015).
[6] M. Campisi and R. Fazio, The power of a critical heat engine, Nat. Commun. **7**, 11895 (2016).
[7] K. Zhang, F. Bariani, and P. Meystre, Quantum optomechanical heat engine, Phys. Rev. Lett. **112**, 150602 (2014).

[8] T. Feldmann and R. Kosloff, Performance of discrete heat engines and heat pumps in finite time, Phys. Rev. E **61**, 4774 (2000).
[9] E. Geva and R. Kosloff, A quantum-mechanical heat engine operating in finite time. A model consisting of spin-1/2 systems as the working fluid, J. Chem. Phys. **96**, 3054 (1992).
[10] R. J. de Assis, J. S. Sales, U. C. Mendes, and N. G. de Almeida, Two-level quantum Otto heat engine operating with unit efficiency far from the quasi-static regime under a squeezed reservoir, J. Phys. B: At. Mol. Opt. Phys. **54**, 095501 (2021).
[11] J. Roßnagel, O. Abah, F. Schmidt-Kaler, K. Singer, and E. Lutz, Nanoscale heat engine beyond the Carnot limit, Phys. Rev. Lett. **112**, 030602 (2014).
[12] O. Abah, J. Roßnagel, G. Jacob, S. Deffner, F. Schmidt-Kaler, K. Singer, and E. Lutz, Single-ion heat engine at maximum power, Phys. Rev. Lett. **109**, 203006 (2012).
[13] N. M. Myers and S. Deffner, Bosons outperform fermions: The thermodynamic advantage of symmetry, Phys. Rev. E **101**, 012110 (2020).
[14] J. Klaers, S. Faelt, A. Imamoglu, and E. Togan, Squeezed thermal reservoirs as a resource for a nanomechanical engine beyond the Carnot limit, Phys. Rev. X **7**, 031044 (2017).
[15] J. Wang, Z. Wu, and J. He, Quantum Otto engine of a two-level atom with single-mode fields, Phys. Rev. E **85**, 041148 (2012).
[16] T. Feldmann and R. Kosloff, Characteristics of the limit cycle of a reciprocating quantum heat engine, Phys. Rev. E **70**, 046110 (2004).
[17] X. L. Huang, H. Xu, X. Y. Niu, and Y. D. Fu, A special entangled quantum heat engine based on the two-qubit Heisenberg *XX* model, Phys. Scr. **88**, 065008 (2013).
[18] X. L. Huang, Y. Liu, Z. Wang, and X. Y. Niu, Special coupled quantum Otto cycles, Eur. Phys. J. Plus **129**, 4 (2014).
[19] E. A. Ivanchenko, Quantum Otto cycle efficiency on coupled qudits, Phys. Rev. E **92**, 032124 (2015).
[20] N. M. Myers, O. Abah, and S. Deffner, Quantum Otto engines at relativistic energies, New J. Phys. **23**, 105001 (2021).
[21] H. Wang, S. Liu, and J. He, Performance analysis and parametric optimum criteria of an irreversible Bose–Otto engine, J. Appl. Phys. **105**, 083534 (2009).
[22] N. M. Myers, F. J. Peña, O. Negrete, P. Vargas, G. De Chiara, and S. Deffner, Boosting engine performance with Bose–Einstein condensation, New J. Phys. **24**, 025001 (2022).
[23] F. Altintas, A. Ċ. Hardal, and Ö. E. Müstecaplıoğlu, Rabi model as a quantum coherent heat engine: From quantum biology to superconducting circuits, Phys. Rev. A **91**, 023816 (2015).
[24] Q. Song, S. Singh, K. Zhang, W. Zhang, and P. Meystre, One qubit and one photon: The simplest polaritonic heat engine, Phys. Rev. A **94**, 063852 (2016).
[25] G. A. Barrios, F. Albarrán-Arriagada, F. A. Cárdenas-López, G. Romero, and J. C. Retamal, Role of quantum correlations in light-matter quantum heat engines, Phys. Rev. A **96**, 052119 (2017).
[26] B. Mojaveri, A. Dehghani, and Z. Ahmadi, A quantum correlated heat engine based on the parity-deformed Jaynes–Cummings model: Achieving the classical Carnot efficiency by a local classical field, Phys. Scr. **96**, 115102 (2021).
[27] E. T. Jaynes and F. W. Cummings, Comparison of quantum and semiclassical radiation theories with application to the beam maser, Proc. IEEE **51**, 89 (1963).
[28] D. Braak, Integrability of the Rabi model, Phys. Rev. Lett. **107**, 100401 (2011).
[29] Q. H. Chen, C. Wang, S. He, T. Liu, and K. L. Wang, Exact solvability of the quantum Rabi model using Bogoliubov operators, Phys. Rev. A **86**, 023822 (2012).
[30] D. Braak, Q. H. Chen, M. T. Batchelor, and E. Solano, Semi-classical and quantum Rabi models: In celebration of 80 years, J. Phys. A: Math. Theor. **49**, 300301 (2016).
[31] I. I. Rabi, On the process of space quantization, Phys. Rev. **49**, 324 (1936).
[32] I. I. Rabi, Space quantization in a gyrating magnetic field, Phys. Rev. **51**, 652 (1937).
[33] H.-G. Xu, J. Jin, N. G. de Almeida, and G. D. de Moraes Neto, Exploring the role of criticality in the quantum Otto cycle fueled by the anisotropic quantum Rabi-Stark model, Phys. Rev. B **110**, 134318 (2024).

[34] H.-G. Xu, J. Jin, G. D. M. Neto, and N. G. de Almeida, Universal quantum Otto heat machine based on the Dicke model, Phys. Rev. E **109**, 014122 (2024).
[35] H. T. Quan, Y. D. Wang, Y. X. Liu, C. P. Sun, and F. Nori, Maxwell's demon assisted thermodynamic cycle in superconducting quantum circuits, Phys. Rev. Lett. **97**, 180402 (2006).
[36] A. O. Niskanen, Y. Nakamura, and J. P. Pekola, Information entropic superconducting microcooler, Phys. Rev. B **76**, 174523 (2007).
[37] J. P. Pekola, V. Brosco, M. Möttönen, P. Solinas, and A. Shnirman, Decoherence in adiabatic quantum evolution: Application to Cooper pair pumping, Phys. Rev. Lett. **105**, 030401 (2010).
[38] J. V. Koski, A. Kutvonen, I. M. Khaymovich, T. Ala-Nissila, and J. P. Pekola, On-chip Maxwell's demon as an information-powered refrigerator, Phys. Rev. Lett. **115**, 260602 (2015).
[39] J. P. Pekola, D. S. Golubev, and D. V. Averin, Maxwell's demon based on a single qubit, Phys. Rev. B **93**, 024501 (2016).
[40] J. Roßnagel, S. T. Dawkins, K. N. Tolazzi, O. Abah, E. Lutz, F. Schmidt-Kaler, and K. Singer, A single-atom heat engine, Science **352**, 325 (2016).
[41] G. Maslennikov, S. Ding, R. Hablützel, J. Gan, A. Roulet, S. Nimmrichter, J. Dai, V. Scarani, and D. Matsukevich, Quantum absorption refrigerator with trapped ions, Nat. Commun. **10**, 202 (2019).
[42] K. Zhang, F. Bariani, and P. Meystre, Theory of an optomechanical quantum heat engine, Phys. Rev. A **90**, 023819 (2014).
[43] O. Fialko and D. Hallwood, Isolated quantum heat engine, Phys. Rev. Lett. **108**, 085303 (2012).
[44] J. P. Brantut, C. Grenier, J. Meineke, D. Stadler, S. Krinner, C. Kollath, T. Esslinger, and A. Georges, A thermoelectric heat engine with ultracold atoms, Science **342**, 713 (2013).
[45] T. B. Batalhão, A. M. Souza, L. Mazzola, R. Auccaise, R. S. Sarthour, I. S. Oliveira, J. Goold, G. De Chiara, M. Paternostro, and R. M. Serra, Experimental reconstruction of work distribution and study of fluctuation relations in a closed quantum system, Phys. Rev. Lett. **113**, 140601 (2014).
[46] K. Micadei, J. P. S. Peterson, A. M. Souza, R. S. Sarthour, I. S. Oliveira, G. T. Landi, T. B. Batalhão, R. M. Serra, and E. Lutz, Reversing the direction of heat flow using quantum correlations, Nat. Commun. **10**, 2456 (2019).
[47] R. J. de Assis, T. M. de Mendonça, C. J. Villas-Boas, A. M. de Souza, R. S. Sarthour, I. S. Oliveira, and N. G. de Almeida, Efficiency of a quantum Otto heat engine operating under a reservoir at effective negative temperatures, Phys. Rev. Lett. **122**, 240602 (2019).
[48] Q. Bouton, J. Nettersheim, S. Burgardt, D. Adam, E. Lutz, and A. Widera, A quantum heat engine driven by atomic collisions, Nat. Commun. **12**, 2063 (2021).
[49] M. D. Alsulami and M. Y. Abd-Rabbou, Quantum heat engines with spin-chain-star systems, Ann. Phys. **536**, 2400122 (2024).
[50] A. Ü. C. Hardal and Ö. E. Müstecaplıoğlu, Superradiant quantum heat engine, Sci. Rep. **5**, 12953 (2015).
[51] J. Jaramillo, M. Beau, and A. del Campo, Quantum supremacy of many-particle thermal machines, New J. Phys. **18**, 075019 (2016).
[52] Y.-Y. Chen, G. Watanabe, Y.-C. Yu, X.-W. Guan, and A. del Campo, An interaction-driven many-particle quantum heat engine and its universal behavior, npj Quantum Inf. **5**, 88 (2019).
[53] F. Carollo, F. M. Gambetta, K. Brandner, J. P. Garrahan, and I. Lesanovsky, Nonequilibrium quantum many-body Rydberg atom engine, Phys. Rev. Lett. **124**, 170602 (2020).
[54] T. Fogarty and T. Busch, A many-body heat engine at criticality, Quantum Sci. Technol. **6**, 015003 (2021).
[55] N. Yunger Halpern, C. D. White, S. Gopalakrishnan, and G. Refael, Quantum engine based on many-body localization, Phys. Rev. B **99**, 024203 (2019).
[56] R. Uzdin, Coherence-induced reversibility and collective operation of quantum heat machines via coherence recycling, Phys. Rev. Appl. **6**, 024004 (2016).
[57] W. Niedenzu and G. Kurizki, Cooperative many-body enhancement of quantum thermal machine power, New J. Phys. **20**, 113038 (2018).
[58] K. Menon, T. Busch, and T. Fogarty, Leveraging quantum statistics to enhance heat engines, Quantum Sci. Technol. **10**, 045039 (2025).
[59] J. Koch, K. Menon, E. Cuestas, S. Barbosa, E. Lutz, T. Fogarty, T. Busch, and A. Widera, A quantum engine in the BEC–BCS crossover, Nature (London) **621**, 723 (2023).

[60] E. Q. Simmons, R. Sajjad, K. Keithley, H. Mas, J. L. Tanlimco, E. Nolasco-Martinez, Y. Bai, G. H. Fredrickson, and D. M. Weld, Thermodynamic engine with a quantum degenerate working fluid, Phys. Rev. Res. **5**, L042009 (2023).
[61] R. H. Dicke, Coherence in spontaneous radiation processes, Phys. Rev. **93**, 99 (1954).
[62] M. J. Bhaseen, J. Mayoh, B. D. Simons, and J. Keeling, Dynamics of nonequilibrium Dicke models, Phys. Rev. A **85**, 013817 (2012).
[63] M. Greiner, O. Mandel, T. Esslinger, T. W. Hänsch, and I. Bloch, Quantum phase transition from a superfluid to a Mott insulator in a gas of ultracold atoms, Nature (London) **415**, 39 (2002).
[64] M. J. Hwang, R. Puebla, and M. B. Plenio, Quantum phase transition and universal dynamics in the Rabi model, Phys. Rev. Lett. **115**, 180404 (2015).
[65] P. Nataf and C. Ciuti, No-go theorem for superradiant quantum phase transitions in cavity QED and counter-example in circuit QED, Nat. Commun. **1**, 72 (2010).
[66] J. Klinder, H. Keßler, M. Reza Bakhtiari, M. Thorwart, and A. Hemmerich, Observation of a superradiant Mott insulator in the Dicke-Hubbard model, Phys. Rev. Lett. **115**, 230403 (2015).
[67] A. D. Greentree, C. Tahan, J. H. Cole, and L. C. L. Hollenberg, Quantum phase transitions of light, Nat. Phys. **2**, 856 (2006).
[68] M. J. Hartmann, F. G. S. L. Brandão, and M. B. Plenio, Strongly interacting polaritons in coupled arrays of cavities, Nat. Phys. **2**, 849 (2006).
[69] M. J. Hartmann, F. G. S. L. Brandão, and M. B. Plenio, Quantum many-body phenomena in coupled cavity arrays, Laser Photon. Rev. **2**, 527 (2008).
[70] S. C. Lei and R. K. Lee, Quantum phase transitions of light in the Dicke-Bose-Hubbard model, Phys. Rev. A **77**, 033827 (2008).
[71] Y. Lu and C. Wang, Influence of counter-rotating interaction on quantum phase transition in Dicke-Hubbard lattice: An extended coherent-state approach, Quantum Inf. Process. **15**, 4347 (2016).
[72] P. Kirton, M. M. Roses, J. Keeling, and E. G. Dalla Torre, Introduction to the Dicke model: From equilibrium to nonequilibrium, and *vice versa* (Adv. Quantum Technol. 1-2/2019), Adv. Quantum Technol. **2**, 1970013 (2019).
[73] M. Schiró, M. Bordyuh, B. Öztop, and H. E. Türeci, Quantum phase transition of light in the Rabi–Hubbard model, J. Phys. B: At. Mol. Opt. Phys. **46**, 224021 (2013).
[74] Q. H. Chen, Y. Y. Zhang, T. Liu, and K. L. Wang, Numerically exact solution to the finite-size Dicke model, Phys. Rev. A **78**, 051801 (2008).
[75] Q. H. Chen, T. Liu, Y. Y. Zhang, and K. L. Wang, Quantum phase transitions in coupled two-level atoms in a single-mode cavity, Phys. Rev. A **82**, 053841 (2010).
[76] T. Ye, C. Wang, and Q. H. Chen, Quantum phase transition of light in the dissipative Rabi-Hubbard lattice: A dressed-master-equation perspective, Phys. Rev. A **104**, 053708 (2021).
[77] A. Le Boité, M.-J. Hwang, H. Nha, and M. B. Plenio, Fate of photon blockade in the deep strong-coupling regime, Phys. Rev. A **94**, 033827 (2016).
[78] A. Settineri, V. Macrí, A. Ridolfo, O. Di Stefano, A. F. Kockum, F. Nori, and S. Savasta, Dissipation and thermal noise in hybrid quantum systems in the ultrastrong-coupling regime, Phys. Rev. A **98**, 053834 (2018).
[79] F. Beaudoin, J. M. Gambetta, and A. Blais, Dissipation and ultrastrong coupling in circuit QED, Phys. Rev. A **84**, 043832 (2011).
[80] C. W. Gardiner and M. J. Collett, Input and output in damped quantum systems: Quantum stochastic differential equations and the master equation, Phys. Rev. A **31**, 3761 (1985).
[81] H. T. Quan, Quantum thermodynamic cycles and quantum heat engines. II., Phys. Rev. E **79**, 041129 (2009).
[82] T. D. Kieu, The second law, Maxwell's demon, and work derivable from quantum heat engines, Phys. Rev. Lett. **93**, 140403 (2004).
[83] A. Solfanelli, M. Falsetti, and M. Campisi, Nonadiabatic single-qubit quantum Otto engine, Phys. Rev. B **101**, 054513 (2020).
[84] H. Spohn, Entropy production for quantum dynamical semigroups, J. Math. Phys. **19**, 1227 (1978).

[85] S. Deffner and E. Lutz, Nonequilibrium entropy production for open quantum systems, Phys. Rev. Lett. **107**, 140404 (2011).

[86] P. Forn-Díaz, L. Lamata, E. Rico, J. Kono, and E. Solano, Ultrastrong coupling regimes of light-matter interaction, Rev. Mod. Phys. **91**, 025005 (2019).

[87] A. Frisk Kockum, A. Miranowicz, S. De Liberato, S. Savasta, and F. Nori, Ultrastrong coupling between light and matter, Nat. Rev. Phys. **1**, 19 (2019).